Supporting Information Appendix

Juhas *et al.*

Appendix Contents:

1) SI Materials and Methods

Cell Isolation and GCaMP3 Transduction. Muscle tissue from the lower hind limbs of 2-3-d-old Sprague-Dawley rats was digested with 1 mg/mL collagenase (Worthington) and 2% dispase ((v/v), BD) in Wyles solution (Table S1) for 1 h at 37°C on a rocker, as previously described (1). Isolated cells were resuspended in growth medium (Table S1), and preplated for 2 h at 37°C to reduce fraction of faster-adhering fibroblasts. The supernatant was then seeded on Matrigel coated flasks, and following day cells were reconstituted in growth media, transduced with a GCaMP3 lentivirus, and after 24 h, detached by 2% dispase (v/v) and used for generation of engineered muscle bundles. The implanted GCaMP3^{+} muscle bundles were identified following staining with anti-GFP (Abcam) antibody.

Engineering of Muscle Bundles. Large single muscle bundles and smaller tri-bundle muscle implants were formed within polydimethylsiloxane (PDMS) molds containing a single semi-cylindrical well (1.25 cm long, 3 mm diameter) or three semi-cylindrical wells (7 mm long, 2 mm diameter), respectively, cast from 3D-machined Teflon masters. PDMS molds were coated with 0.2% (w/v) pluronic (Invitrogen) to prevent hydrogel adhesion. For single bundles, two Velcro felts (2mm x 4mm) were pinned at ends of the wells to anchor the hydrogel. Similarly, for tri-bundle implants, laser-cut Cerex® frames (9 mm x 9 mm, 1 mm wide rim) positioned around the 3 wells enabled hydrogel attachment and facilitated construct handling and implantation. Cell/hydrogel mixture (Table S1) was injected into the PDMS wells, polymerized at 37°C for 45 min, and cultured on a rocker at 37°C for 2-4 wk. After 4 d of culture, growth medium was replaced by differentiation medium (Table S1) to promote fusion and differentiation of the myogenic cells into myofibers. Degradation of fibrin was inhibited by 1 mg/mL aminocaproic acid (Sigma). Cell-mediated hydrogel compaction generated passive tension resulting in uniaxial cell alignment (2, 3).

Implantation of Engineered Muscle Bundles. All animal experiments were approved by the Duke University ACUC. Nude mice (~10 wk of age; 22-30 g) were anesthetized by intraperitoneal injection of ketamine (100 mg/kg) and xylazine (10 mg/kg). Using aseptic technique, the dorsal skin was attached to a temporary "C-frame" at the center of the back. The skin was perforated in three locations to accommodate the screws of the chamber, and a circular region (~12 mm) of the forward-facing skin (i.e., cutis, subcutis, retractor and panniculus carnosis muscles, and associated fascia) was dissected away to accommodate the window proper. The forward and rearward pieces of the titanium dorsal skinfold chamber were assembled together from opposite sides of the skin, and a Cerex® frame with tri-bundle muscle constructs was laid perpendicular (verified under microscope) to the intact panniculus carnosis muscle of the rearward-facing skin (Fig. S12*F-G*), providing a source of microvessels for vascularization. A sterile cover glass was placed over the window and engineered tissue while superfusing with sterile saline solution. The chamber was then secured with suture and the “C-frame” was removed. Post-operatively, the mouse was injected subcutaneously with buprenorphine (1 mg/kg) painkiller and let to recover on a heating pad (4).

Intravital Imaging of Blood Vessels. Intravital recordings were performed in anesthetized mice on d 2, 5, 7, 9, 12, and 14 post-implantation (PI). Mice were anesthetized by nose cone

inhalation of isoflurane and positioned on a heating pad under a microscope objective. Hyperspectral brightfield image sequences (10 nm increments from 500 – 600 nm) were captured at 5x magnification using a tunable filter (Cambridge Research & Instrumentation, Inc.) and a DVC camera (ThorLabs), as previously described (4). A custom MATLAB (MathWorks) script was applied to create maps of total hemoglobin concentration (Fig. S15). Obtained maps were further processed using local contrast enhancement in ImageJ (FIJI) and thresholded to binary images to identify vessel area and calculate blood vessel density (BVD, total area of blood vessels per bundle area).

Intravital Imaging of Intracellular Ca^{2+} Transients. Intravital imaging of spontaneous Ca^{2+} transients was performed immediately after vessel imaging with mice still anesthetized. Fluorescent GCaMP3 signals in implanted bundles were video-imaged through a FITC-filter using a fast fluorescent camera (Andor; at 16 μm spatial and 20 ms temporal resolution). Amplitudes of spontaneous Ca^{2+} transients were determined using the Solis software (Andor) by averaging relative fluorescence intensity (ΔF/F) from three ~400x400 μm^2 regions within each bundle (Fig. S12*C*) (5).

In Vitro and Ex Vivo Measurements of Ca^{2+} Transients. Electrically-induced GCaMP3 Ca^{2+} transients were imaged in engineered muscle bundles after 2 and 14 d of in vitro culture and in muscle explants 1 and 2 wk PI. Engineered muscle constructs were transferred into a custom chamber mounted on an inverted fluorescence microscope (Nikon), placed in 37°C Tyrode's solution (Table S1), and electrically stimulated (10 ms pulse, 3 V/mm). Induced GCaMP3 signals were recorded using a fast fluorescent camera Andor iXon 860 EMCCD (24 μm spatial and 20 ms temporal resolution) and analyzed as described for intravital assessment. Kinetics of Ca^{2+} transients were also characterized as previously described (5).

Immunostaining. Cultured cells were fixed in 4% paraformaldehyde (PFA, 15 min, RT). Whole muscle constructs and native muscle tissues were fixed overnight (4°C) in 2% PFA. Fixed samples were washed in PBS, and placed in blocking solution (Table S1) overnight (4°C). Samples were incubated in primary antibodies (Table S2) for 24 h (4°C), washed in PBS, and incubated in secondary antibodies (Table S2) for 2 h (37°C). Images were acquired using a Zeiss confocal microscope. Tissues used for cross-sectional staining were embedded in paraffin, sectioned (5 μm), washed with xylene, rehydrated, microwaved 5 times for 3 m in a citrate buffer solution (Table S1), and immunostained.

Analysis of Nuclear Counts. To automate nuclear counting, we utilized a custom MATLAB image processing program (6) that allows user-thresholding of DAPI or transcription factor (Pax7, Ki67, MyoD, myogenin) staining and, based on the median size of nuclei for a given magnification, designates and counts identified nuclei. The program outputs the processed images with identified nuclei for the manual verification by user.

Analysis of Myofiber and Blood Vessel Alignment. Orientation of muscle fibers (marked by expression of GFP or F-actin) and blood vessels (marked by expression of CD31) was quantified in engineered muscle implants and native muscle from confocal images acquired at 20x magnification using a previously described image intensity gradient algorithm (3, 6). Local feature orientation was calculated within 25x25 pixel (11x11 μm) subregions (Fig. S8) in which

myofibers or blood vessels were present and standard vessel angle deviation and absolute mean fiber angle difference between myofiber and vessel directions were calculated by averaging subregion data over the entire (450x450 μm) image. Four images were analyzed per each muscle sample.

Statistics. Results are presented as mean ± SEM. Statistical significances among different groups were evaluated by unpaired t-test or one-way ANOVA with post hoc Tukey's test using GraphPad Prism (GraphPad Software, Inc.). $P<0.05$ was consider statistically significant. Different levels of significance were noted in figures and figure captions.

References

1. Bian W & Bursac N (2009) Engineered skeletal muscle tissue networks with controllable architecture. *Biomaterials* 30(7):1401-1412.
2. Hinds S, Bian W, Dennis RG, & Bursac N (2011) The role of extracellular matrix composition in structure and function of bioengineered skeletal muscle. *Biomaterials* 32(14):3575-3583.
3. Bian W, Liau B, Badie N, & Bursac N (2009) Mesoscopic hydrogel molding to control the 3D geometry of bioartificial muscle tissues. *Nature protocols* 4(10):1522-1534.
4. Palmer GM*, et al.* (2011) In vivo optical molecular imaging and analysis in mice using dorsal window chamber models applied to hypoxia, vasculature and fluorescent reporters. *Nature protocols* 6(9):1355-1366.
5. Bian W & Bursac N (2012) Soluble miniagrin enhances contractile function of engineered skeletal muscle. *FASEB journal : official publication of the Federation of American Societies for Experimental Biology* 26(2):955-965.
6. Badie N, Satterwhite L, & Bursac N (2009) A method to replicate the microstructure of heart tissue in vitro using DTMRI-based cell micropatterning. *Annals of biomedical engineering* 37(12):2510-2521.

2) SI Tables.

Table S1. Cell Culture Media and Solutions

Name	Details
Blocking solution	5% chicken serum, 0.2% Triton-X (Sigma)
Cell/hydrogel mixture	10 million cells/mL, 2x growth medium, 4 mg/mL bovine fibrinogen (Sigma), Matrigel (20% v/v)), thrombin (0.2 unit/mg fibrinogen, Sigma)
Citrate Buffer Solution	90% H_2O, 8% 100mM Sodium Citrate, 2% 100mM Citric Acid
Differentiation Medium	DMEM, 3% (v/v) horse serum, 50 unti/mL penicillin G, 50 ug/mL strepomycin, 5 ug/mL gentamicin
Growth Medium	Dulbecco's modified Eagle's medium (DMEM), 10% (v/v) fetal bovine serum, 50 unti/mL penicillin G, 50 ug/mL strepomycin, 5 ug/mL gentamicin
Tyrode's Solution	135 mM NaCl, 5.4 mM KCl, 1.8 mM CaCl, 1 mM MgCl, 0.33 mM NaHPO, 5 mM HEPES, 5 mM glucose
Wyles Solution	137 mM NaCl, 5 mM KCl, 21 mM HEPES, 0.7 mM Na2HPO4, 100 mM glucose, 0.1 mg/mL BSA

Table S2. Antibody List

Primary Epitope	Dilution	Supplier	Catalog no.
Pax7	1:15	Developmental Studies Hybridoma Bank	Pax7-s
MyoD	1:200	BD Pharmingen	554130
myogenin	1:200	Santa Cruz Biotechnology	sc-576
sarcomeric α-actinin	1:200	Sigma	a7811
collagen IV	1:300	Abcam	ab6586
laminin	1:300	Abcam	ab11575
vimentin	1:400	Sigma	v6630
CD31	1:300	Abcam	ab28364
VWF	1:200	Abcam	ab6994
Ki67	1:200	Abcam	Ab15580
Secondary Epitope	**Dilution**	**Supplier**	**Catalog no.**
Alexa Fluor 488 Phalloidin	1:300	Life Technologies	A12379
Alexa Fluor 594 Chicken Anti-Mouse IgG	1:200	Life Technologies	A21201
Alexa Fluor 594 Chicken Anti-Rabbit IgG	1:201	Life Technologies	A21442
Alexa Fluor 647 Chicken Anti-Mouse IgG	1:202	Life Technologies	A21463
Alexa Fluor 488 Chicken Anti-Mouse IgG	1:203	Life Technologies	A21200

3) SI Figures

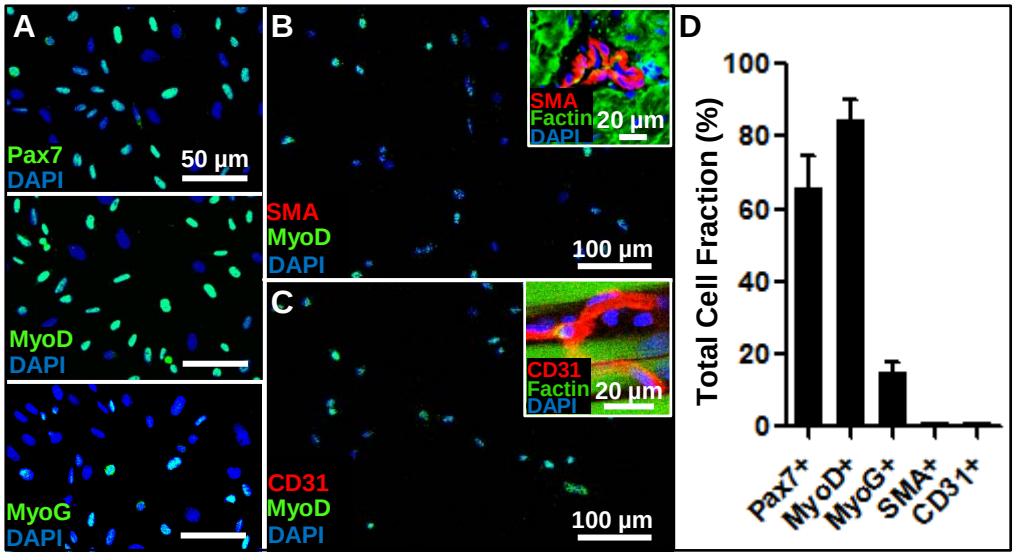

Fig. S1. Input cell population for engineering of skeletal muscle bundles. (*A*) Representative immunostaining of Pax7$^+$, MyoD$^+$, and myogenin (MyoG)$^+$ cells. (*B-C*) No α-smooth muscle actin (SMA)$^+$ smooth muscle cells (*A*) or CD31$^+$ endothelial cells (*B*) were present in the cell isolates. Insets, positive controls for SMA and CD31 antibodies showing a blood vessel in adult rat cardiac muscle (*A*) and capillaries in native neonatal rat skeletal muscle (*B*). (*D*) Quantified fractions of myogenic (Pax7$^+$, MyoD$^+$, MyoG$^+$) and vasculogenic (SMA$^+$, CD31$^+$) cells used for engineering of skeletal muscle (n = 3 cell isolations). Stainings suggest that cell population consists primarily of activated satellite cells (SCs), a proliferative population of Pax7$^+$/MyoD$^+$ cells that can either commit to a myoblast fate (Pax7$^-$/MyoD$^+$) or revert to the quiescent state (Pax7$^+$/MyoD$^-$) characteristic of homeostatic native muscle.

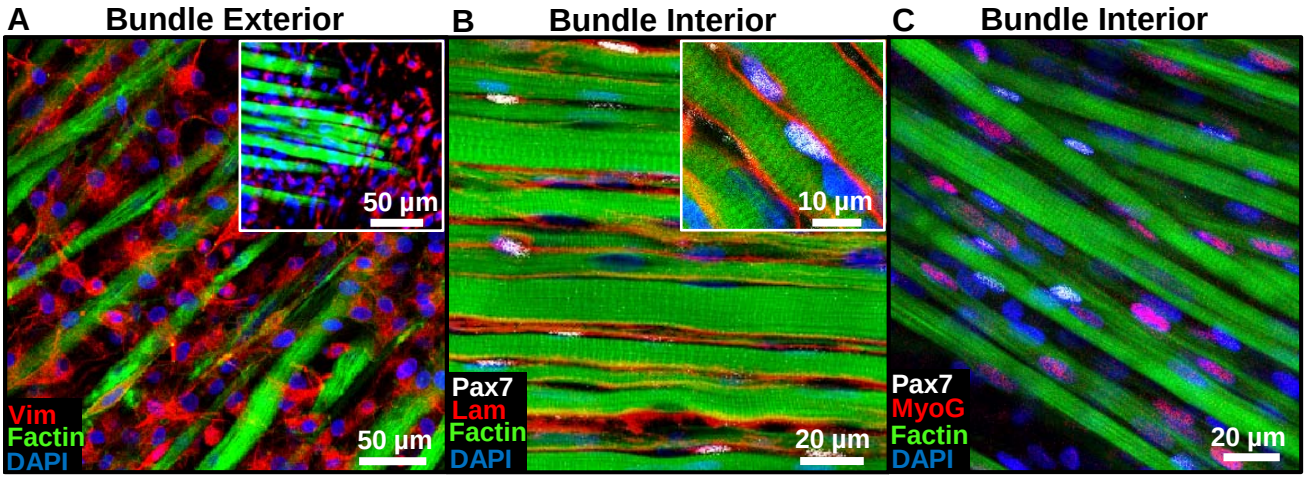

Fig. S2. Structural organization of engineered muscle bundles. (*A*) Representative image of the exterior of a 2-wk old engineered muscle bundle showing an outer layer of vimentin$^+$ fibroblasts; inset: staining of the epimysial region of the neonatal rat soleus muscle showing similar fibroblast abundance. (*B*) Representative image of the interior of a 2-wk old engineered muscle bundle consisting of aligned striated myofibers and abutting Pax7$^+$ satellite cells (SCs) residing within a laminin-rich (Lam) matrix; inset: close-up of neonatal rat soleus muscle showing similar position of SCs beneath basal lamina. (*C*) Representative image of the distribution of SCs and myonuclei (MyoG$^+$ nuclei) in a 2-wk old engineered muscle bundle.

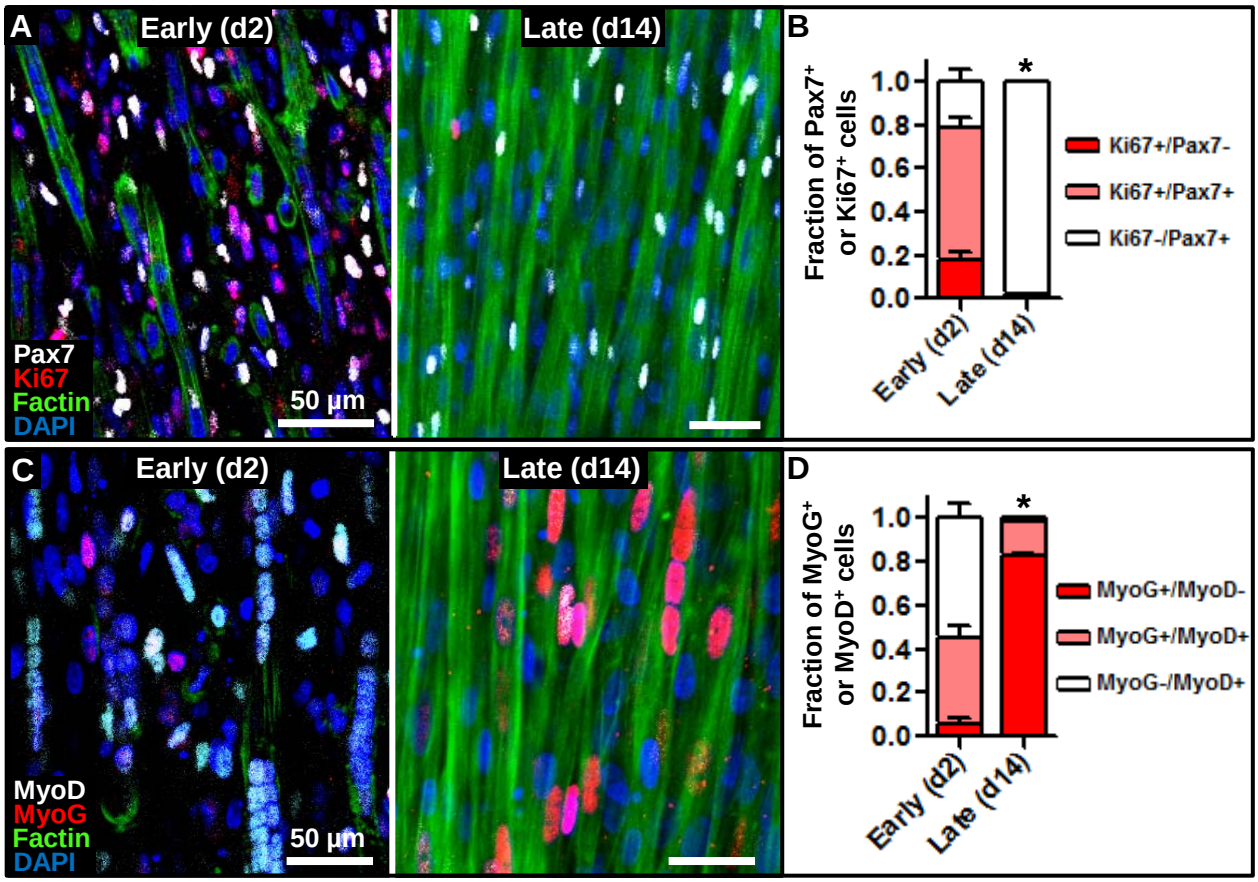

Fig. S3. Acquisition of homeostatic cell composition within engineered muscle bundles. (*A*) Representative images of Pax7 and Ki67 expression inside the engineered muscle bundles at early fusion (2d) and late post-differentiation (14d) times during in vitro culture. (*B*) Quantified fractions of $Pax7^+$ and/or $Ki67^+$ cells at 2 and 14 days of culture. Note a homeostatic shift to a non-proliferative quiescent muscle phenotype at 14d of culture. (*C*) Representative MyoD and myogenin (MyoG) expression inside the engineered muscle bundles at 2 and 14 days of culture. Note that abundant expression of MyoD in early fusing myofibers at culture day 2 is significantly decreased with the formation of mature myofibers by day 14. (*D*) Quantified fractions of $MyoD^+$ and/or $MyoG^+$ cells demonstrate switch to a mature, differentiated muscle phenotype. Mean ± SEM; *n* = 3-6 bundles per group; P*<0.05 compared to corresponding early time-point for each group.

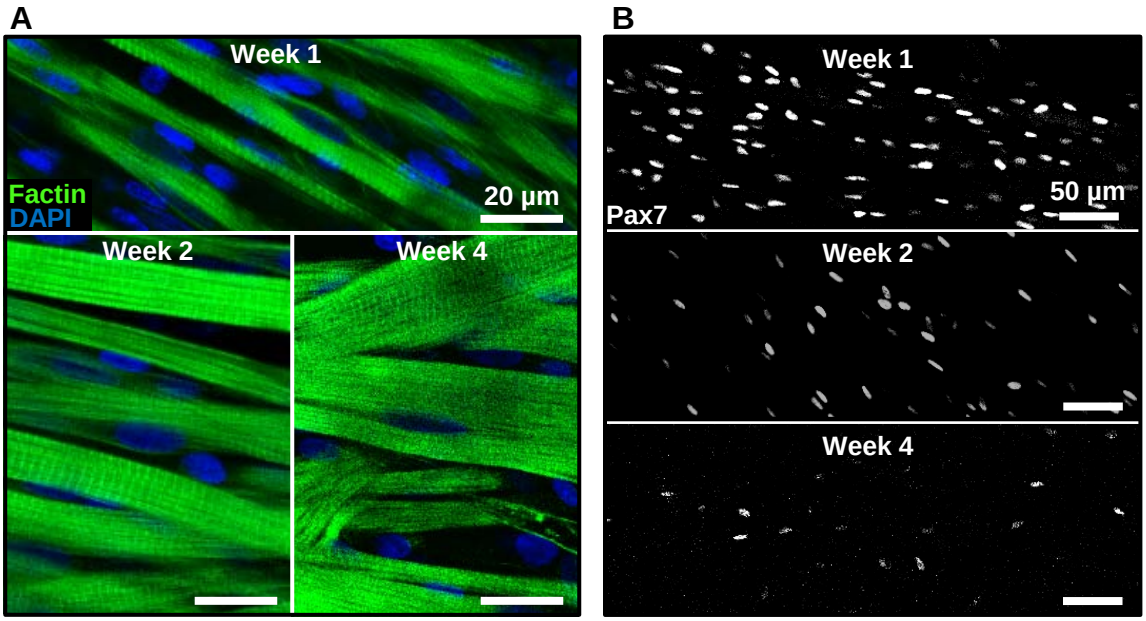

Fig. S4. Myofiber hypertrophy in engineered muscle bundles. (*A*,*B*) Representative images of the steady increase in myofiber diameter (*A*) and decrease in Pax7$^+$ SC number (*B*) within engineered muscle bundles over 4 wk culture.

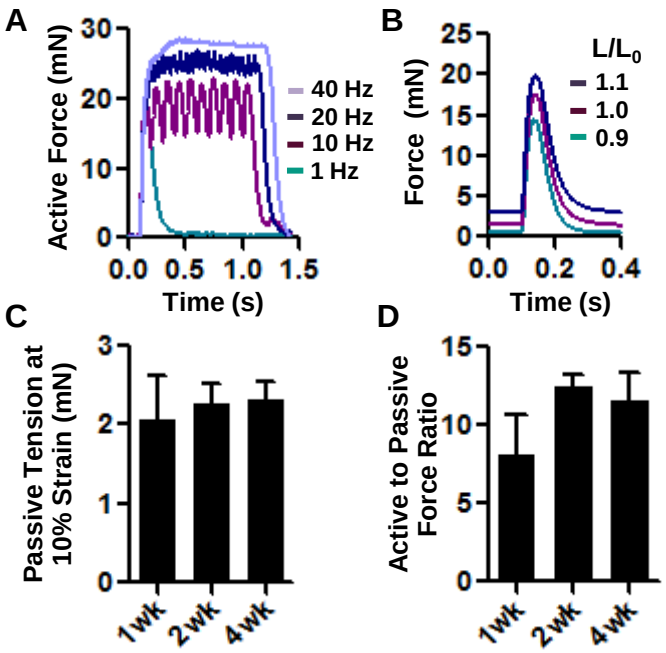

Fig. S5. Functional characterization of engineered muscle bundles. (*A*) Representative active force traces in 2-wk old engineered muscle bundles showing increase in active force amplitude and generation of tetanic contraction at increased frequency of electrical stimulation. (*B*) Representative twitch force traces in 2-wk old engineered muscle bundles showing changes in active twitch and passive tension amplitudes with increase in engineered muscle length L (relative to initial length L_0). (*C*) Amplitude of passive tension at 10% strain (L/L_0=1.1). (*D*) Ratio of active tetanus force to passive tension amplitudes at 10% strain. Mean ± SEM; *n* = 4-10 bundles per group.

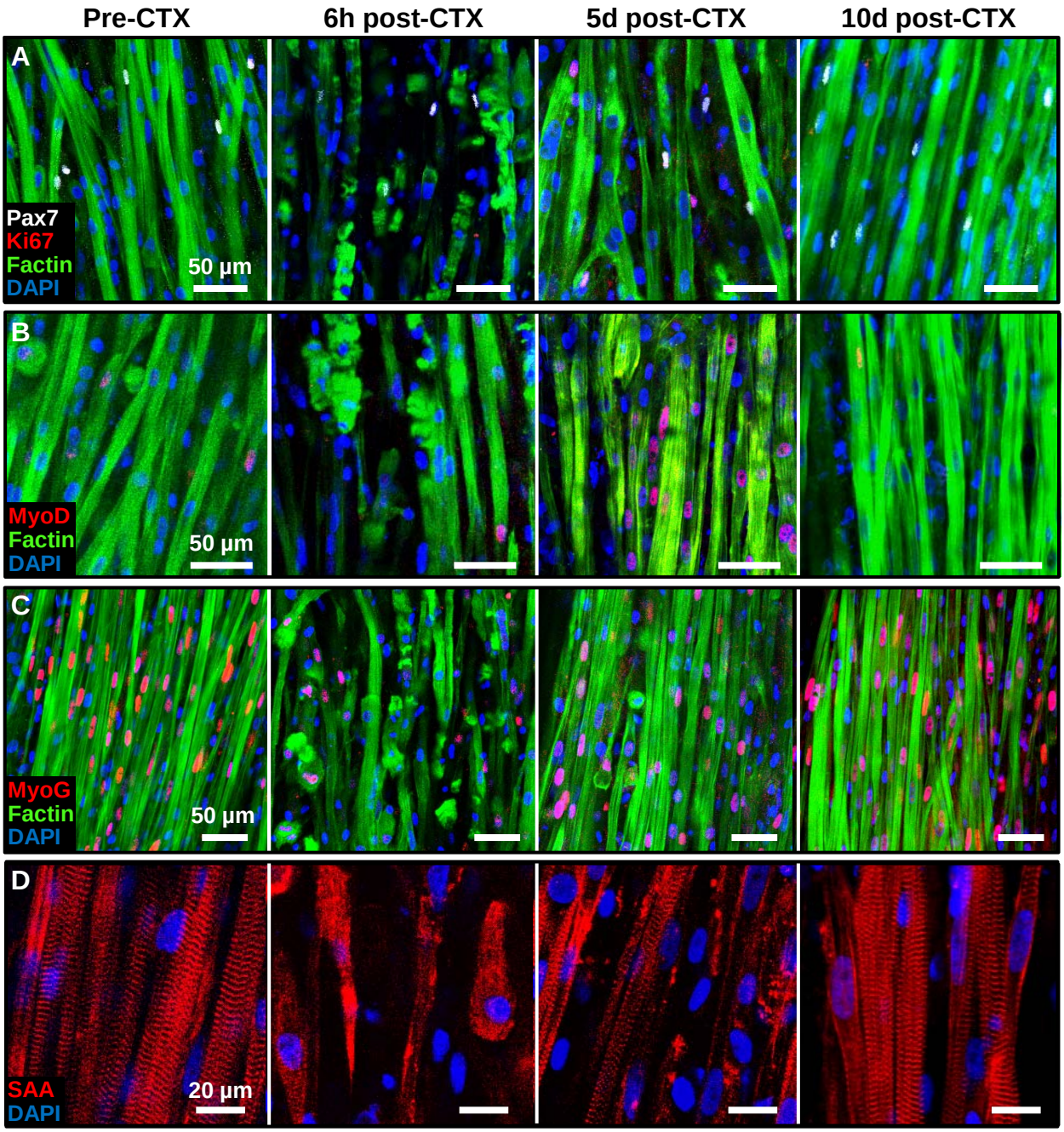

Fig. S6. Regeneration of engineered muscle bundles following cardiotoxin injury in vitro. (*A-C*) Representative images of proliferating satellite cells ($Pax7^{+}/Ki67^{+}$) (*A*), MyoD (*B*), and myogenin (MyoG) (*C*) in 2-wk old engineered muscle bundles prior to cardiotoxin (CTX) administration and 6 hours, 5 days, and 10 days after CTX injury. (*D*) Representative images of the immediate sarcomere destruction following CTX injury and the gradual recovery of sarcomeric structures over the following 10 days of culture.

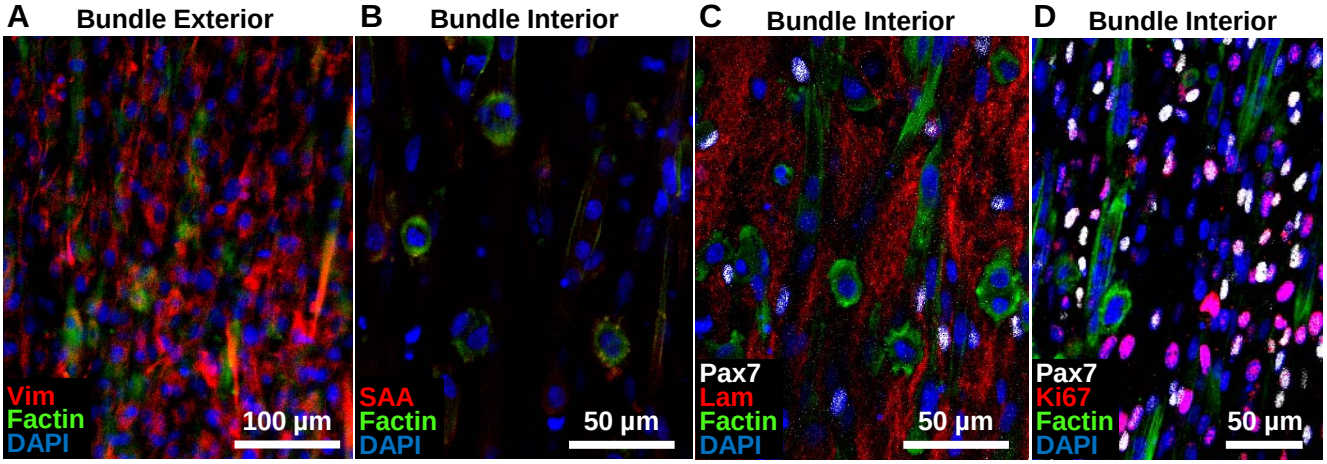

Fig. S7. Structural characterization of 2-day old undifferentiated engineered (UnD) muscle bundles. (*A*) Vimentin (Vim)$^{+}$ fibroblasts were predominantly found at the exterior of the bundle. (*B-C*) Non-fused or newly fusing myogenic cells as well as short immature myotubes were found within the interior of bundle (*B*), along with Pax7^{+} cells and a laminin (Lam)-rich matrix (*C*). *(D)* Undifferentiated myogenic cells inside the bundle were highly proliferative, as evident by the abundant expression of Ki67.

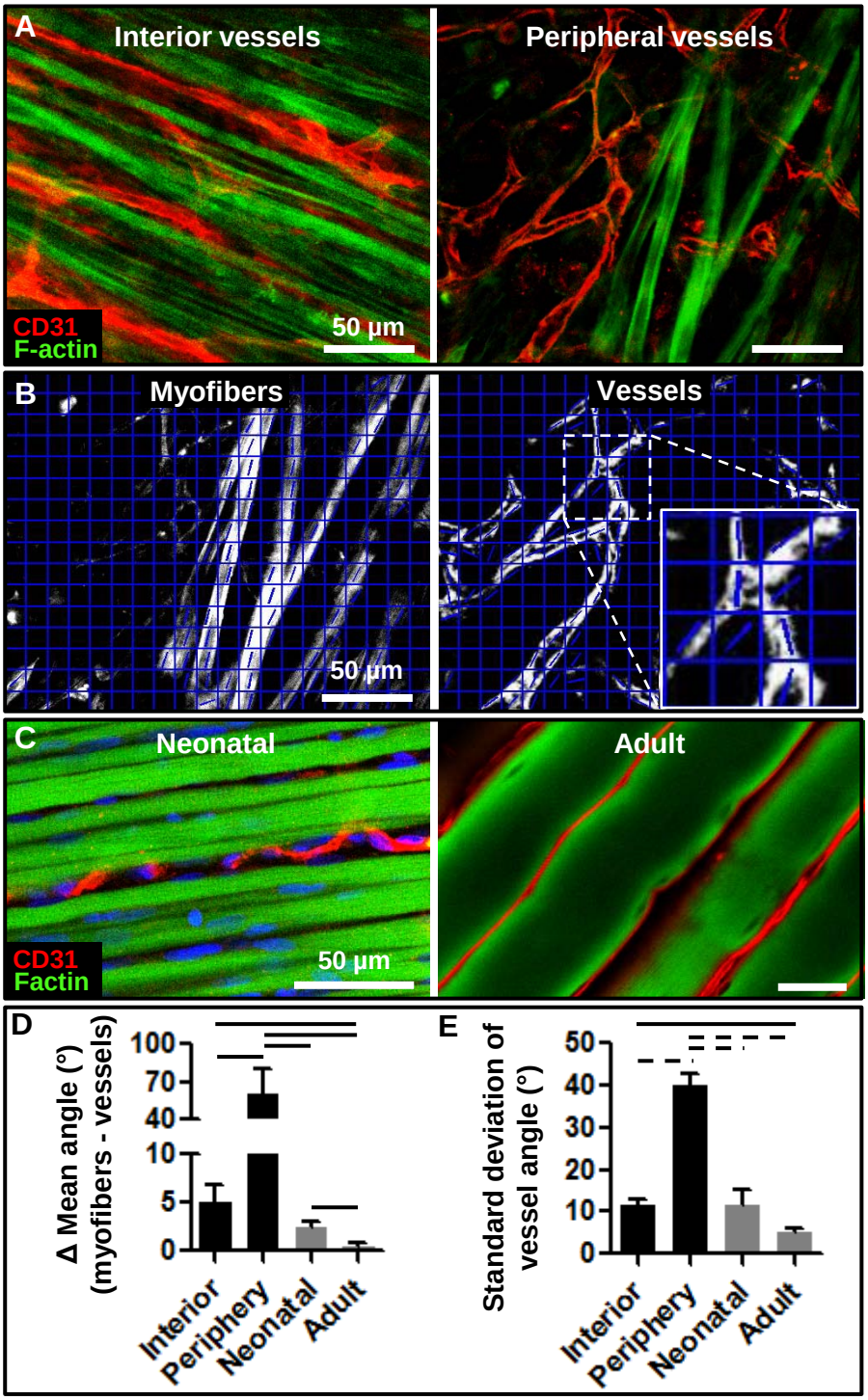

Fig. S8. Vascular organization in implanted engineered muscle bundles. (*A*) Representative images of CD31$^+$ blood vessels and GFP$^+$ myofibers in the interior and periphery of the pre-differentiated (PreD) muscle bundles at 2 wk post-implantation (PI). (*B*) Processed panel A (right) showing separated green and red channels with local myofiber and vessel directions quantified within individual 25x25 pixel (11x11 μm) regions. The close-up inset shows mean direction (angle) of alignment within each pixel denoted by a thin line. (*C*) Representative images of CD31$^+$ vessels in the interior of neonatal and adult muscle. (*D*) Standard deviations of vessel alignment within the interior and periphery of the 2wk PI bundles and native muscles. (*E*) Mean angle differences between average myofiber and vessel directions of alignment. Mean ± SEM; n = 4-8 samples per group (8-10 images per sample); $P<0.05$ and $P<0.001$ between groups denoted by solid and dashed horizontal lines, respectively.

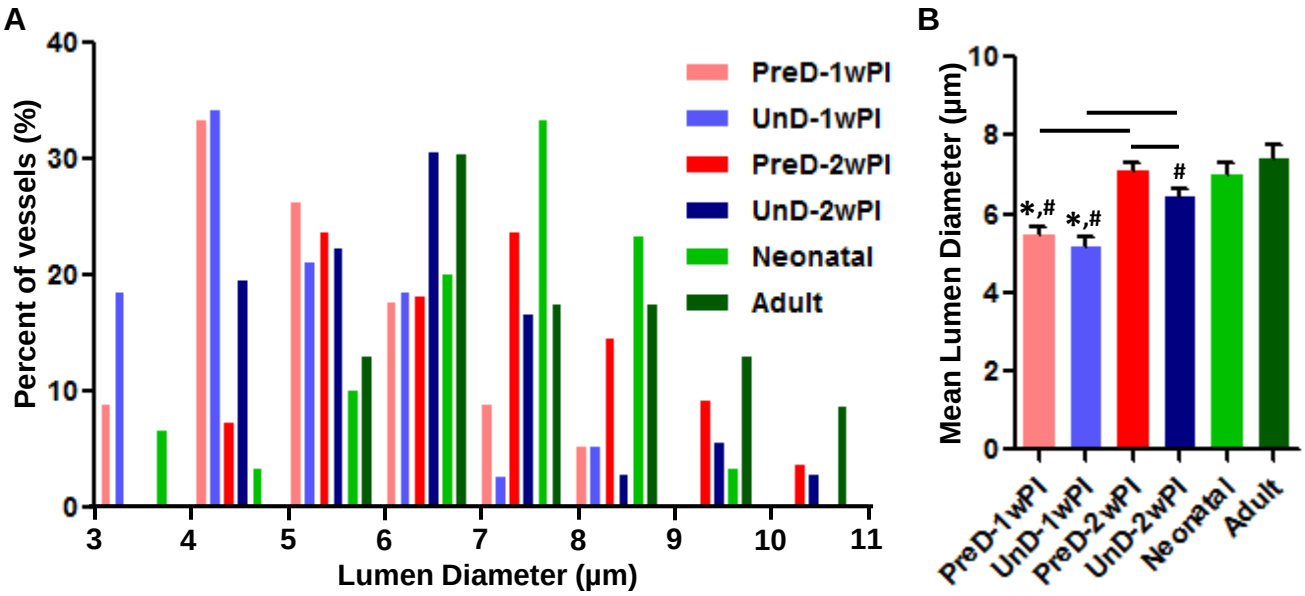

Fig. S9. Capillary lumen diameters in implanted engineered muscle bundles. (*A*) Histogram distribution of lumen diameters within the implanted pre-differentiated (PreD) and undifferentiated (Und) engineered muscle at 1 wk (1wPI) and 2 wk (2wPI) post-implantation (PI) as well in neonatal and adult hind limb muscles. Capillary lumen diameters were measured from cross-sectional images immunostained with F-actin and Von Willebrand Factor (example shown in Figure 3E). (*B*) Mean lumen diameters in 6 studied groups. Mean ± SEM; *n* = 50-70 lumens per group; *P < 0.001 compared to neonatal values, $^{\#}$P < 0.05 compared to adult values, and P < 0.05 between groups denoted by horizontal lines.

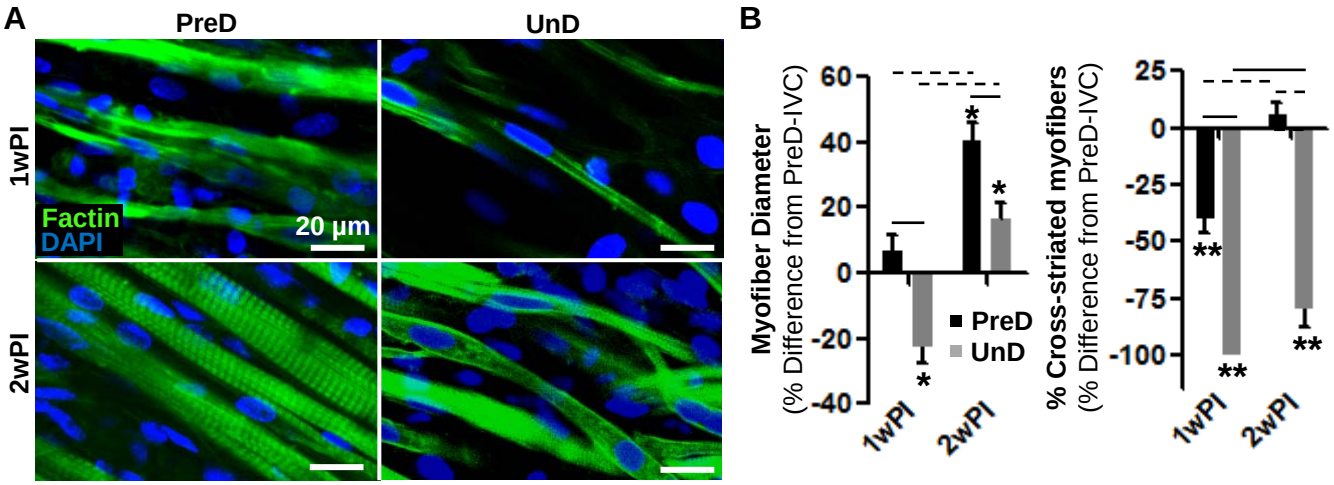

Fig. S10. Myogenesis and structural differentiation of implanted engineered muscle bundles. (*A*) Representative images of myofibers within implanted pre-differentiated (PreD) and undifferentiated (UnD) muscle bundles at 1 wk (1wPI) and 2 wk (2wPI) post-implantation. (*B*) Changes in myofiber diameter and percent of cross-striated myofibers relative to values in PreD bundles cultured for 2 wk *in vitro* (PreD-IVC). Mean ± SEM; *n* = 8-12 bundles (10-20 measurements per bundle) per group; *P<0.05 and **P<0.001 compared to PreD-IVC values; P<0.01 and P<0.001 between groups denoted by solid and dashed horizontal lines, respectively.

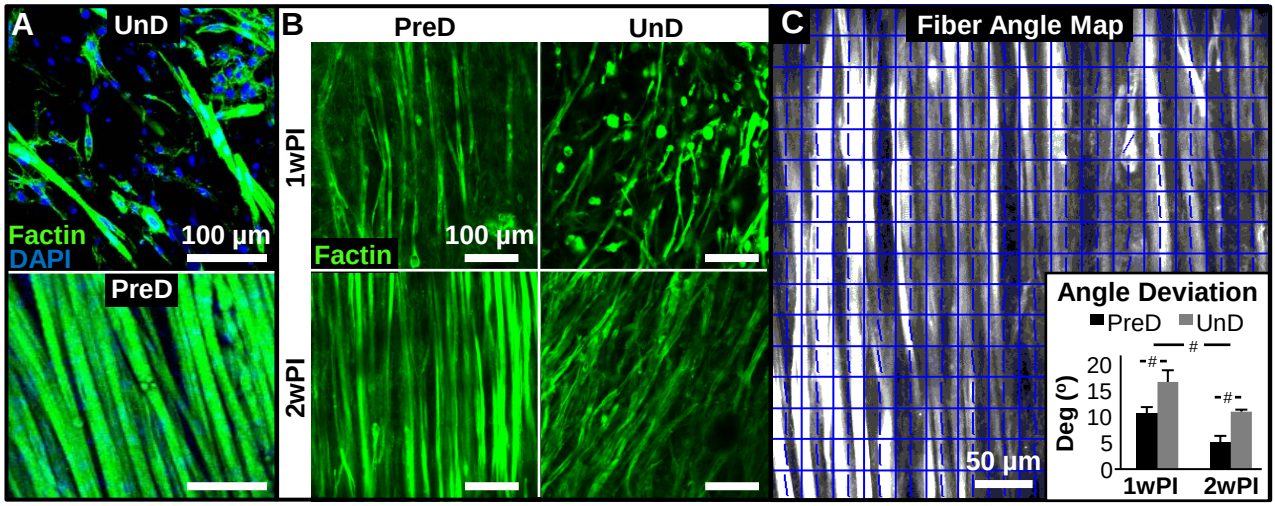

Fig. S11. Myofiber alignment in pre-differentiated and undifferentiated implanted engineered muscle bundles. (*A*) Representative images of myofibers in undifferentiated (UnD) and pre-differentiated (PreD) engineered muscle bundles prior to implantation. (*B*) Representative images of myofiber alignment in PreD and UnD bundles at 1 (1wPI) and 2 wk (2wPI) post-implantation. (*C*) Example map of local myofiber directions within 25x25 pixel (11x11 µm) regions in a PreD bundle. Inset, average local angle deviation from mean myofiber direction (in units of deg). Note more uniform unidirectional alignment (smaller angle deviation) in PreD vs. UnD group. Mean ± SEM, n = 4 bundles per group, $^{\#}P < 0.01$.

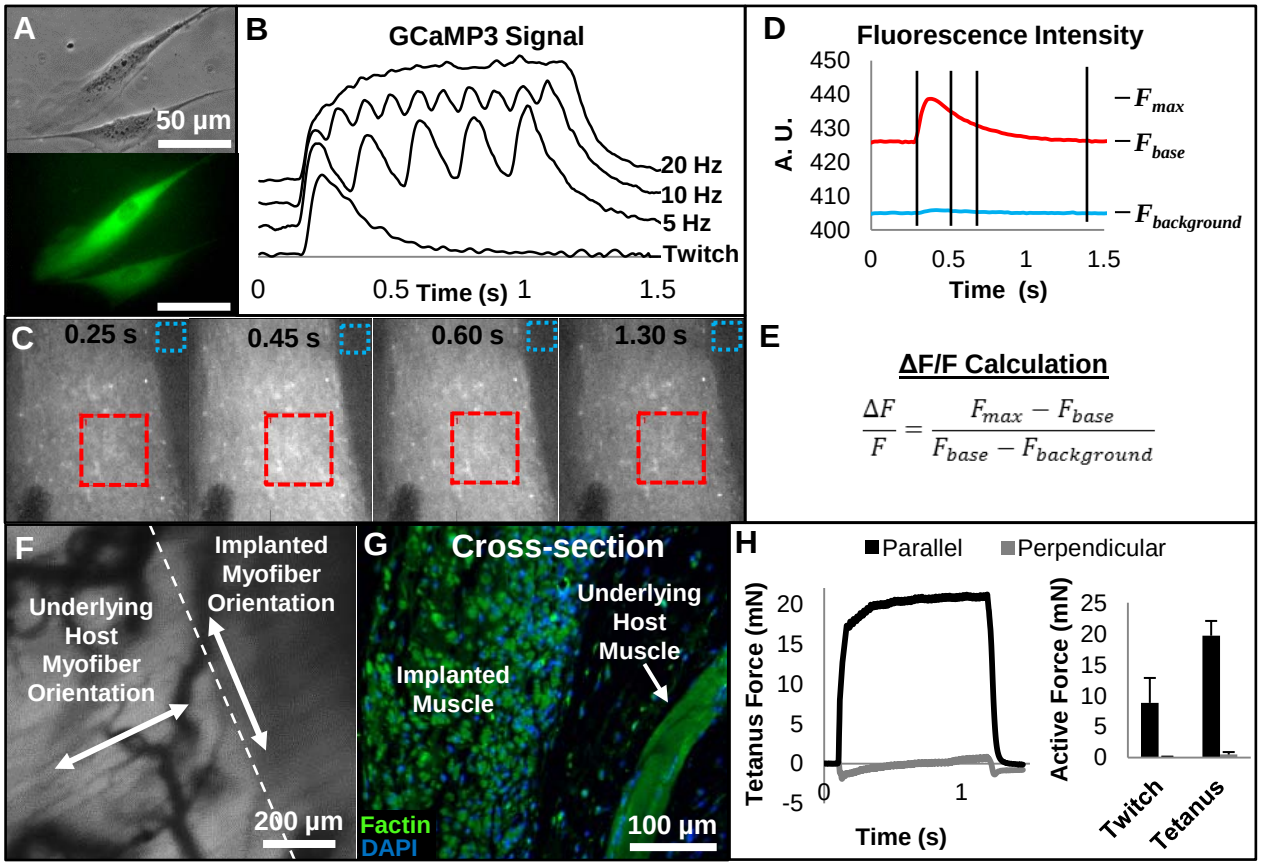

Fig. S12. Measurements of intracellular calcium transient and contractile force generation in implanted engineered muscle bundles. (*A*) Representative brightfield and fluorescent images of myogenic cells transduced with GCaMP3 virus prior to assembly into a muscle bundle. (*B*) Representative GCaMP3 traces from an engineered muscle bundle at various stimulation frequencies. The traces are progressively shifted upwards for improved clarity. (*C*) Select time snapshots of recorded GCaMP3 fluorescence from an explanted muscle bundle during application of an electrical stimulus. (*D*) Averaged fluorescence traces from the red square region within the muscle bundle and blue square region (background) outside of the bundle shown in (*C*). Vertical lines denote times of the snapshots shown in (*C*). (*E*) ΔF/F signal amplitude is calculated using the shown formula. (*F*) Representative brightfield image of an engineered muscle bundle implanted perpendicular to the direction of underlying host muscle fibers within a dorsal window chamber. (*G*) 2 wk post-implantation, transverse cross-section of implanted muscle overlaying longitudinal section of host muscle confirms that two muscles remain perpendicular to each other. (*H*) Representative tetanus force traces and average active forces of control host muscle without implant, measured parallel and perpendicular to host myofiber orientation. Note that in the direction perpendicular to host myofiber orientation (and along the orientation of implanted muscle bundles), the active force generated by the host muscle is negligible. Mean ± SEM; *n* = 3 mice.

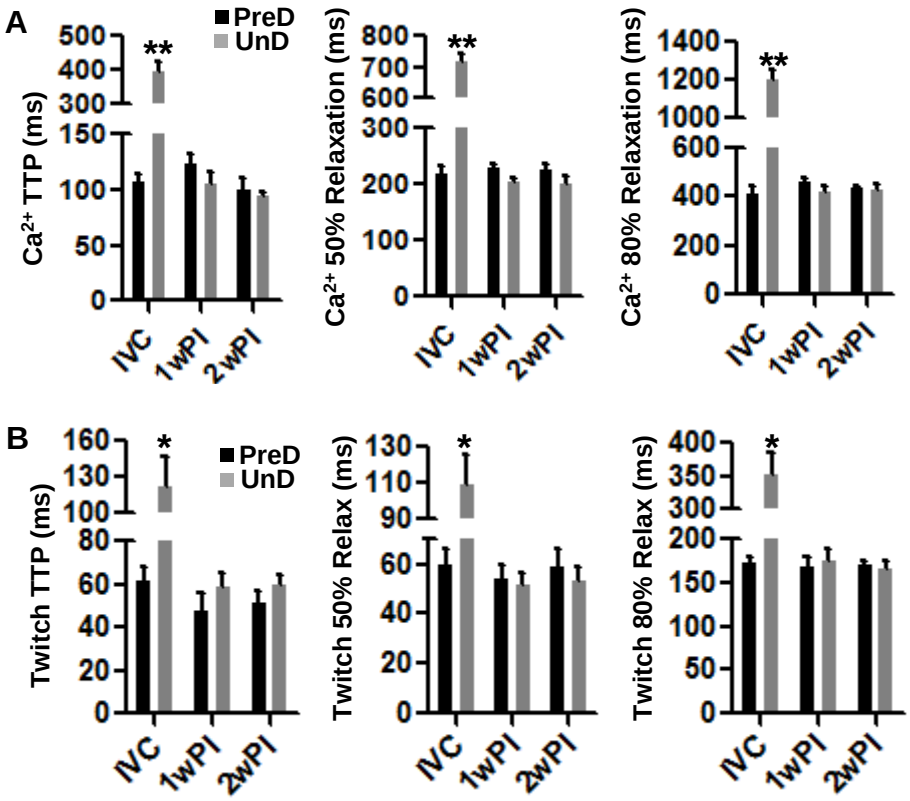

Fig S13. Kinetics of electrically-induced calcium transient and twitch force responses in engineered muscle bundles. Time-to-peak (TTP), 50% relaxation, and 80% relaxation times of (*A*) recorded GCaMP3-calcium transients and (*B*) measured twitch forces during 1 Hz electrical stimulation in pre-differentiated (PreD) and undifferentiated (UnD) *in vitro* (IVC) patches and patches explanted at 1 wk (1wPI) and 2 wk (2wPI) post-implantation. Mean ± SEM; *n* = 6-10 bundles per group; other groups; **P<0.0001 and *P<0.05 compared to all other groups.

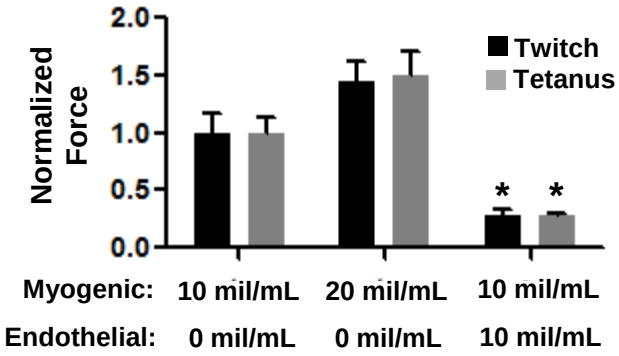

Fig. S14. Effect of co-encapsulation of endothelial and myogenic cells on function of engineered muscle bundles. Twitch and tetanus forces with varying concentrations of myogenic and rat aortic endothelial cells within the engineered muscle bundles normalized to 10 mil/mL myogenic cell group (control). Mean ± SEM; *n* = 4-8 bundles per group; P*<0.01 compared to control.

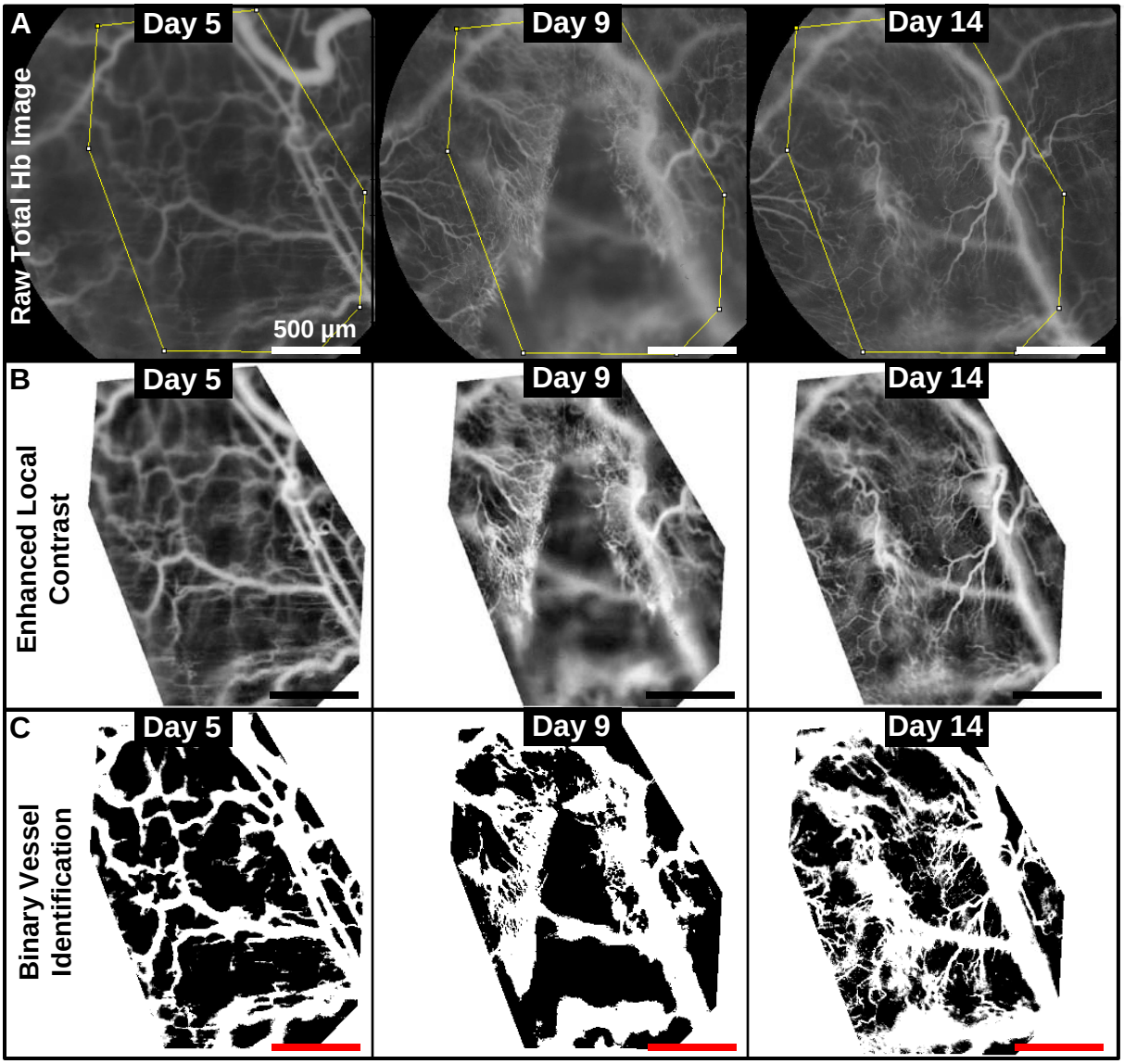

Fig. S15. Method for calculating blood vessel density in implanted engineered muscle bundles. (*A*) Consistent regions of interests (ROIs) were identified within raw intravital images of total hemoglobin concentration for the same implanted bundle at different time points (days) post implantation. Using ImageJ (FIJI) software, local contrast was enhanced (*B*) and blood vessels were identified following conversion of the enhanced into binary images (*C*). From these images, the blood vessel density (i.e., total vessel area per bundle area) was measured in blind fashion.

4) SI Movie Legends

Movie S1. **Engineered muscle contractions.** Representative twitch and tetanus contractions of an unloaded, 2-week old engineered muscle bundle electrically stimulated by a single pulse (10 ms duration, 3 V/mm) or a 40 Hz pulse train, respectively. During culture, ends of the engineered muscle were attached to rectangular Velcro® felts.

Movie S2. Ingrown neovasculature within implanted engineered muscle. Representative intravital recordings of ingrown neovasculature within the implanted engineered muscle (yellow pseudo-color region) at 7 and 14 days post-implantation. Red blood cell flow through the ingrown vessels and spontaneous contractions of engineered muscle are readily observed.

Movie S3. Spontaneous tetanic contraction of implanted engineered muscle. Representative intravital recording of spontaneous tetanic contractions in the implanted engineered muscle (yellow pseudo-color regions) at 14 days post-implantation. Note that during tetanic contraction, blood flow in the ingrown capillaries appears to be transiently haltered.

Movie S4. In vivo recordings of $Ca2^+$ transients. Representative intravital recordings of GCaMP3-reported spontaneous Ca^{2+} transients in the implanted pre-differentiated (PreD) and undifferentiated (UnD) engineered muscle bundles (yellow pseudo-color regions) at 14 days post-implantation. Note asynchronous firing of spontaneous Ca^{2+} transients (GCaMP3 flashes) in different myofibers within the implants. Stronger flashes are followed by more forceful contractions.

Movie S5. Ex vivo recordings of $Ca2^+$ transients. Representative recordings of GCaMP3-reported, electrically-induced Ca^{2+} transients in the PreD and UnD engineered muscles explanted 14 days post-implantation. Single electrical pulse (10 ms duration, 3 V/mm) induces synchronized, spatially uniform firing of Ca^{2+} transient (GCaMP3 flash) rapidly followed by strong twitch contraction.